AJNR Am J Neuroradiol 24:559–566, April 2003

Image-Based Computational Simulation of Flow Dynamics in a Giant Intracranial Aneurysm

David A. Steinman, Jaques S. Milner, Chris J. Norley, Stephen P. Lownie, and David W. Holdsworth

BACKGROUND AND PURPOSE: **Blood flow dynamics are thought to play an important role in the pathogenesis and treatment of intracranial aneurysms; however, hemodynamic quantities of interest are difficult to measure in vivo. This study shows that computational fluid dynamics (CFD) combined with computed rotational angiography can provide such hemodynamic information in a patient-specific and prospective manner.**

METHODS: **A 58-year-old woman presented with partial right IIIrd cranial nerve palsy due to a giant carotid-posterior communicating artery aneurysm that was subsequently coiled. Computed rotational angiography provided high resolution volumetric image data from which the lumen geometry was extracted. This and a representative flow rate waveform were provided as boundary conditions for finite element CFD simulation of the 3D pulsatile velocity field.**

RESULTS: **CFD analysis revealed high speed flow entering the aneurysm at the proximal and distal ends of the neck, promoting the formation of both persistent and transient vortices within the aneurysm sac. This produced dynamic patterns of elevated and oscillatory wall shear stresses distal to the neck and along the sidewalls of the aneurysm. These hemodynamic features were consistent with patterns of contrast agent wash-in during cine angiography and with the configuration of coil compaction observed at 6-month follow-up.**

CONCLUSION: **Anatomic realism of lumen geometry and flow pulsatility is essential for elucidating the patient-specific nature of aneurysm hemodynamics. Such image-based CFD analysis may be used to provide key hemodynamic information for prospective studies of aneurysm growth and rupture or to predict the response of an individual aneurysm to therapeutic options.**

Blood flow dynamics are thought to be an important factor in the pathogenesis and treatment of cerebral aneurysms. A number of specific hemodynamic factors—notably wall shear stress, pressure and mural stress, impingement force, flow rate, and residence time—have been implicated in aneurysm growth and rupture (1). Judicious control of these hemodynamic factors may also govern the outcomes of endovascular therapies (2–4). However, because of the practical difficulties associated with measuring hemodynamic quantities in vivo, it has been difficult to exploit this potentially important information for basic biologic or clinical studies.

To date, the bulk of investigations into aneurysm hemodynamics have been conducted in vitro, using either mathematically idealized models or casts of postmortem specimens. Although the former are convenient for detailed experimental velocity measurement or numerical simulation (5), they allow only a gross understanding of aneurysm hemodynamics that is difficult to extrapolate to individual cases. The latter, on the other hand, although capable of providing hemodynamic information in a patient-specific manner, obviously permits only retrospective analyses. Moreover, as noted by Imbesi and Kerber (6), "the creation of replicas of human vascular abnormalities, particularly aneurysms, is a tedious and technically difficult undertaking."

With the recent convergence of high resolution 3D medical imaging, powerful desktop workstations, and

Received July 22, 2002; accepted after revision September 7.

This work was supported by grants from the Canadian Institutes of Health Research (MPO-53185 and GR-14973) and the Whitaker Foundation (RG-01–0219); salary support provided by the Heart and Stroke Foundation of Canada in the form of New Investigator (D.A.S) and Career Investigator (D.W.H.) Awards.

Parts of this work were presented at the World Congress of Biomechanics, Calgary, Alberta, Canada, August 2002.

From the Imaging Research Laboratories, Robarts Research Institute (D.A.S., J.S.M., C.J.N., S.P.L., D.W.H.), and the Departments of Medical Biophysics (D.A.S., D.W.H.), Diagnostic Radiology (D.A.S., S.P.L., D.W.H.), and Clinical Neurological Sciences (S.P.L.), University of Western Ontario, London, Canada.

Address reprint requests to David A. Steinman, PhD, Imaging Research Laboratories, Robarts Research Institute, 100 Perth Drive, London, Ontario, Canada N6A 5K8.

sophisticated image processing techniques, it is now possible to reliably simulate pulsatile blood flow in anatomically realistic arterial geometries derived from in vivo imaging (7). This makes it possible to now consider *prospective and patient-specific* studies of aneurysm hemodynamics in relation to their pathogenesis and treatment. Toward this ultimate end, we herein present the first such "image-based computational fluid dynamics (CFD)" study of pulsatile flow in an anatomically realistic human aneurysm model derived from in vivo rotational angiography.

Methods

Patient History

A 58-year-old woman presented with a 1-year history of gradually progressive right-sided ptosis and diplopia on leftward and upward gaze. Neurologic examination revealed partial right IIIrd cranial nerve palsy. CT showed an enhancing parasellar mass. Cerebral angiography revealed a giant aneurysm of the right internal carotid artery. Rotational angiography with 3D reconstruction (hereafter referred to as *computed rotational angiography*) showed a wide necked aneurysm arising at the level of the posterior communicating artery. The aneurysm was treated with GDC embolization.

Image Acquisition

Computed rotational angiographic data were acquired on a clinical C-arm angiographic system modified to allow the collection of projections at a rate of 45 degrees or 30 frames/s (8). Images were obtained with a 28-cm field-of-view, acquiring 135 exposures (90 kVp, 234.3 mA, 3 ms) during 4.4 seconds, during a 6-second selective intra-arterial injection of contrast agent. A nonionic, iodinated contrast agent solution (300 mg/mL Omnipaque diluted to 200 mg/mL with heparinized saline) was used, with an injection rate of 3 mL/s. An anatomic mask acquired by using the same parameters without the injection of contrast agent was used to create subtracted images. Digital images were transferred to a Unix network for cone-beam CT reconstruction with a nominal isotropic voxel size of 390 μm. Representative maximum intensity projections through this volumetric data are shown in Figure 1.

Model Construction

The lumen boundary was first semi-automatically extracted from the reconstructed image volume by using a 3D discrete dynamic contour (9). Middle and anterior cerebral arteries were then truncated proximal to perforators or distal branches. A finite element volume mesh was generated by using a commercial mesh generation package. Mesh refinement studies conducted under steady flow conditions indicated that wall shear stress patterns were adequately resolved with slightly >213,000 quadratic tetrahedral finite elements, corresponding to >311,000 nodes having an average spacing of 0.3 mm. This finite element mesh is shown in Figure 1.

Flow Rate Measurement

Pulsatile flow rate measurements were not obtained for this patient at the time of angiography. Instead, flow rates were measured at the right internal carotid artery of a sex-matched and approximately age-matched volunteer by using cine phase contrast-enhanced MR imaging and flow rate analysis techniques described previously (10). The resulting flow rate waveform (Fig 2, *inset*) had average and peak flow rates of 236 and 371 mL/min, respectively, and a period of 909 milliseconds, corresponding to a heart rate of 66 bpm. Considering the measured inlet diameter (4.26 mm) and assumed blood viscosity (3.5 cPoise), the inlet mean Reynolds and Womersley numbers were 336 and 3.0, respectively.

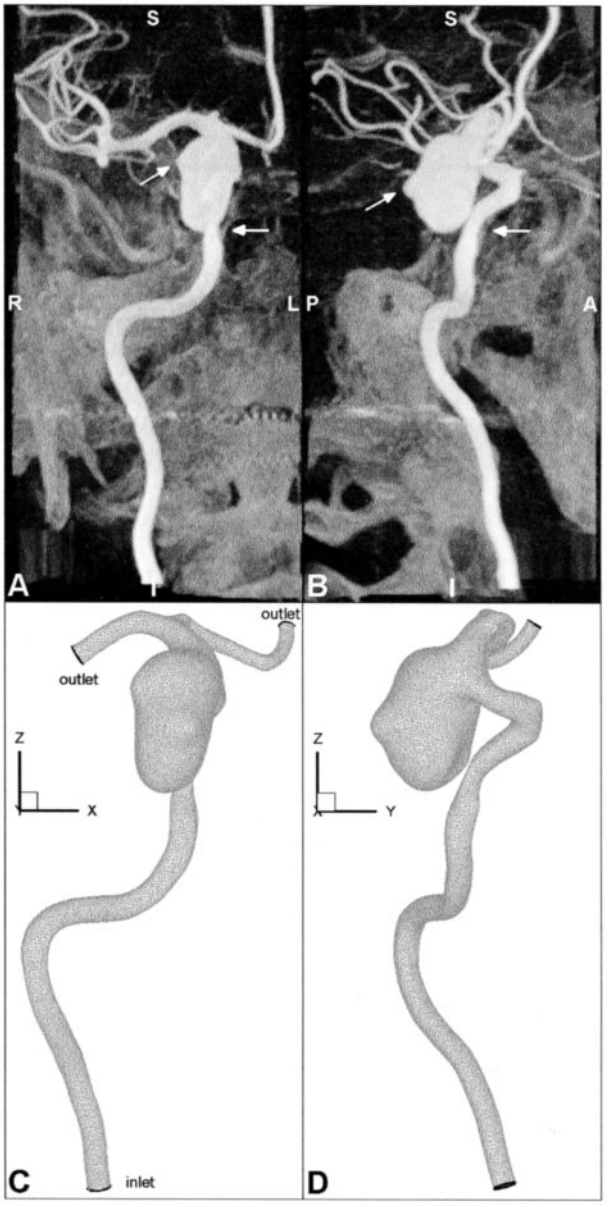

FIG 1. Geometry of aneurysm and parent vessel, shown in anteroposterior (*left column*) and lateral (*right column*) views.

A and *B*, Maximum intensity projections obtained through the CT reconstructed data illustrate the geometrical complexity of the aneurysm and parent vessel. *Angled arrows* identify blebs on the right and posterior sides of the aneurysm sac. *Horizontal arrows* point to an apparent stenosis of the petrous segment, which may be attributed to compression of the vessel against adjacent bone.

C and *D*, Corresponding views of the finite element mesh show the geometric faithfulness and spatial resolution of the CFD model; for clarity, only the corner nodes of the quadratic finite elements are shown. Note the model coordinate system: ± x = left/right, ± y = anterior/posterior, ± z = superior/inferior.

CFD Modeling

CFD simulations were performed by using a well-validated in-house finite element CFD solver (11–13). Rigid walls and

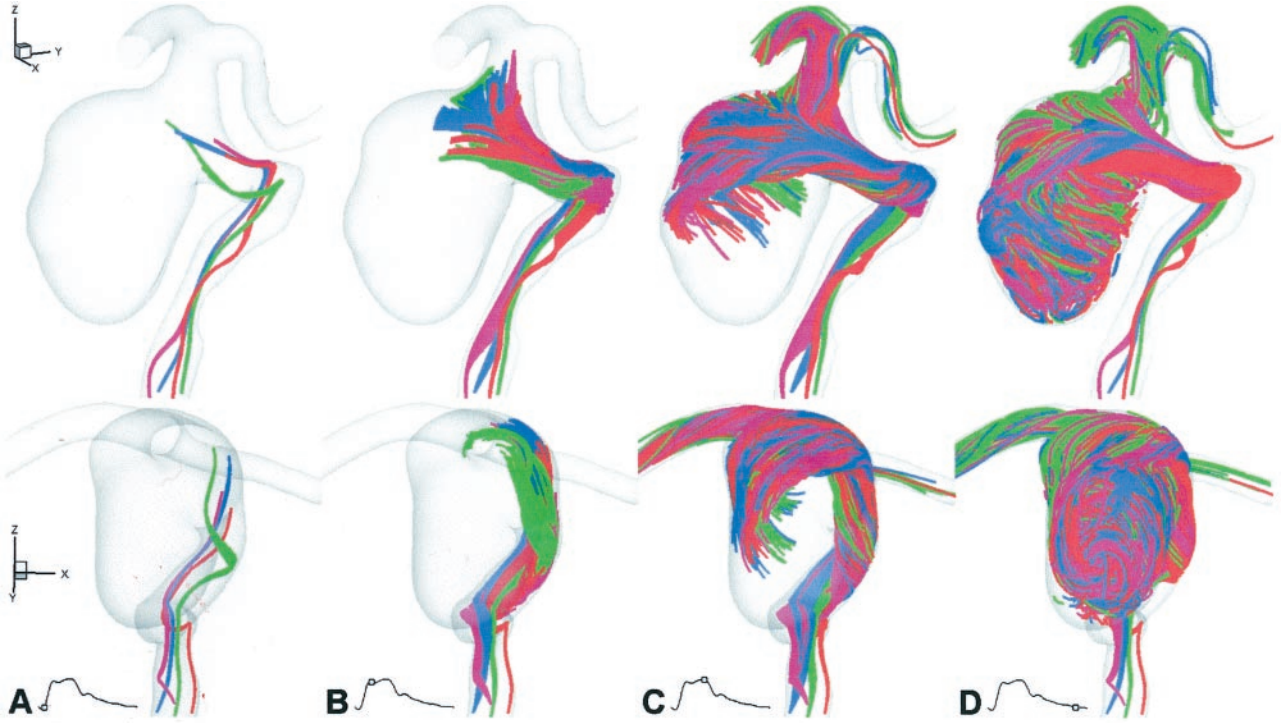

FIG 2. Virtual slipstreams, shown at selected times in lateral (*top row*) and anteroposterior (*bottom row*) oblique views, provide an overview of the aneurysm hemodynamics.

A, Early systole (t = 50 ms). Slipstreams showed little mixing or spreading as they approached the neck.

B, Peak systole (t = 150 ms). Slipstreams spread and began to mix as they entered both the proximal and distal ends of the neck.

C, Early diastole (t = 300 ms). Slipstreams mixed as they impacted the posterior wall of the aneurysm and swirled in the right and inferior directions.

D, Late diastole (t = 800 ms). Within 0.5 second, the aneurysm was almost entirely opacified by vigorously mixed slipstreams.

constant viscosity were assumed. Fully developed velocities were prescribed at the internal carotid artery inlet by weighting Womersley's analytic solution for fully developed pulsatile flow with the Fourier coefficients from the measured flow rate waveform, as described previously (14). Traction-free boundary conditions were applied at the outlets, and equal pressures were assumed. (This resulted in a middle cerebral artery–anterior cerebral artery flow division of 78:22, which was maintained throughout the cardiac cycle.) Pulsatile flow was resolved by using 2400 equally spaced time steps per cardiac cycle; three cycles were required to damp initial transients. Each cycle required approximately 72 hours on a 1-GHz Pentium III workstation.

Flow Visualization

In addition to conventional contour and vector field plots, flow patterns were visualized by using a computational approximation of the slipstream visualization technique used by Imbesi and Kerber (6, 15), Kerber and Heilman (16), and Kerber et al (17, 18) in their experimental studies of aneurysm hemodynamics. Briefly, neutrally buoyant, massless, nondiffusing tracer particles were seeded continuously from within a 2-μm radius at each location of interest and were advected through the CFD-computed velocity field by using particle tracking techniques described previously (19). These "virtual slipstreams" were then visualized by plotting those portions of the resulting trajectories within 250 milliseconds of the time of interest (ie, the effective shutter speed).

Results

The general characteristics of flow in this aneurysm are illustrated in Figure 2 via virtual slipstreams. Before systole, slipstreams converged through the narrowed petrous segment but showed little mixing or spreading as they diverged and approached the aneurysm. At peak systole, slipstreams exhibited more pronounced spreading in the parent vessel and began mixing as they entered the neck from the left side; flow into the proximal neck was direct, whereas the distal neck acted as an effective flow divider. At early diastole, slipstreams continued to mix as they impacted the posterior wall of the aneurysm and then swirled as they decelerated toward the right and inferior directions. By end-diastole slipstreams in the parent vessel again showed little mixing or spreading whereas the aneurysm was almost entirely filled by the vigorously mixed slipstreams. Although difficult to discern from these views, flow was observed exiting the aneurysm in a helical manner, arising from the core rather than the walls of the aneurysm sac, and leaving through the right side of the neck.

A more detailed look at the flow patterns that produced these slipstream dynamics is provided in Figure 3. In particular, flow on the sagittal plane was particularly complex, with patterns varying markedly throughout the cardiac cycle. High speed flow entered the aneurysm superiorly (Fig 3A), traveled along the posterior wall (Fig 3B), and entered into the core of the aneurysm sac (Fig 3C), recirculating further into the aneurysm sac or exiting through the anterior side. This anterior outflow was also evident throughout the cardiac cycle. Two counter-rotating

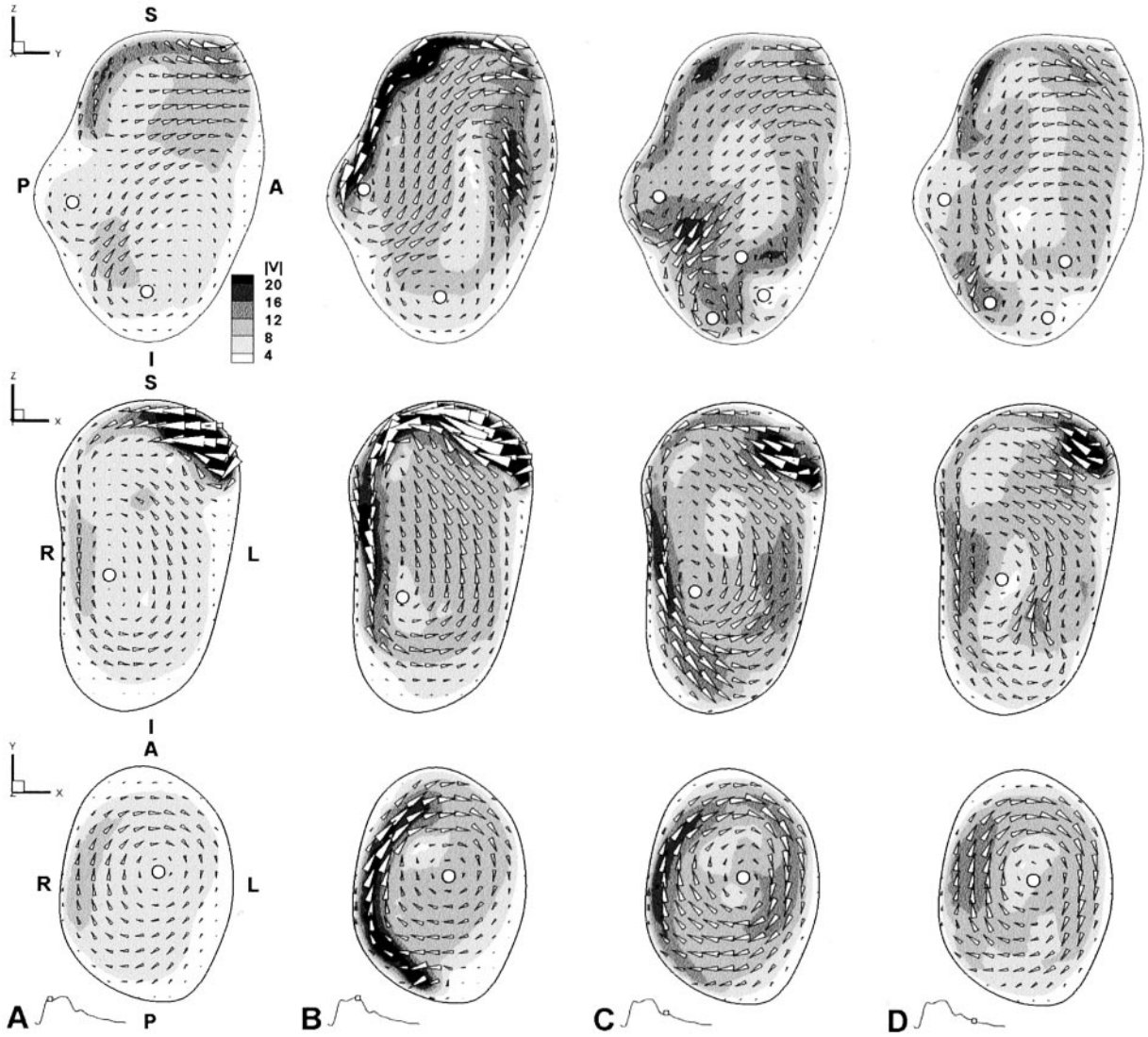

FIG 3. More detailed views of the complex aneurysm hemodynamics are provided at selected times and for selected planes via conventional field plots of sagittal (*top row*), coronal (*middle row*), and axial (*bottom row*) planes, each from the nominal center of the aneurysm. Contours of velocity magnitude (V , in cm/s) are shown with vectors superimposed to indicate the magnitude and direction of in-plane flow components. *White circles* identify the approximate center of each vortex. *S*, superior; *I*, inferior; *A*, anterior; *P*, posterior; *R*, right; *L*, left.

A, Peak systole (t = 150 ms).
B, Early diastole (t = 300 ms).
C, Mid-diastole (t = 450 ms).
D, Late diastole (t = 600 ms).

vortices were also present at the posterior and inferior sides throughout the cardiac cycle, whereas diastolic deceleration induced the formation of two transient and more mobile vortices at the inferior anterior sides. On the coronal plane, high speed flow was seen to enter the aneurysm continuously but with varying speed, from the left superior side. Circulation of flow toward the right and inferior directions around the aneurysm wall was maintained throughout the cardiac cycle, as evidenced by the presence of a vortex, the intensity and center of which varied little during the cardiac cycle. A similarly persistent vortex was also visible on the axial plane, in this case maintained by the swirling of flow from the posterior to anterior sides along the right wall.

The flow patterns detailed above were clearly reflected in the wall shear stress plots shown in Figure 4. Specifically, elevated cycle-averaged shear stresses on the aneurysm wall effectively traced out the trajectory of high speed (and hence higher shear) flow entering the proximal and distal ends of the neck (Fig 4A) and impacting the right wall of the aneurysm before swirling and decelerating inferiorly (Fig 4B). Regions of highly disturbed flow highlighted by elevated oscillatory shear index were particularly evident at the boundaries of the high shear regions, reflecting that high speed flow entering the aneurysm was mobile in the sense that the point of impact on the aneurysm wall migrated during the cardiac cycle. Elevated oscillatory shear index was also seen at the

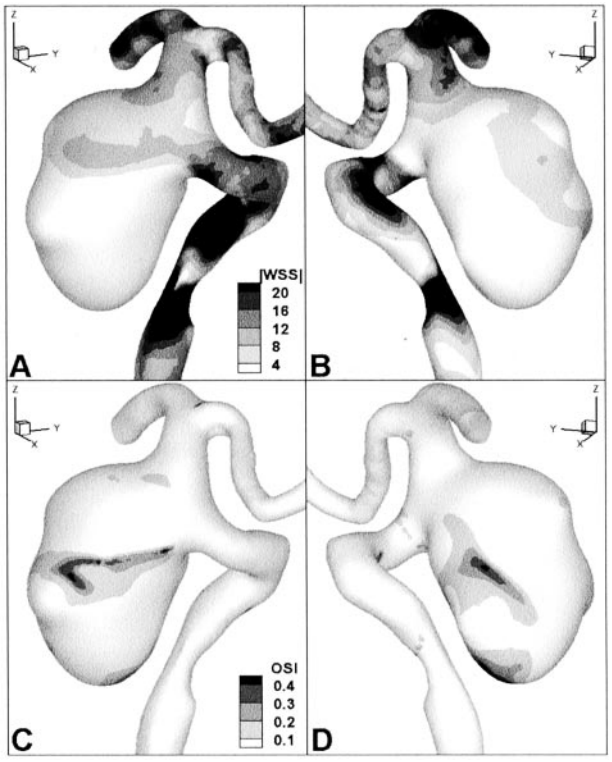

FIG 4. Computed wall shear stress patterns are shown in oblique posterior (*left panels*) and anterior (*right panels*) views.

A and *B*, Contours of cycle-averaged wall shear stress magnitude (WSS , dynes/cm^2).

C and *D*, Contours of oscillatory shear index (*OSI*, dimensionless), a measure of the relative variability of the wall shear stress over the cardiac cycle.

most inferior part of the aneurysm (Fig 4D), the region in which highly mobile and transient vortices were observed.

Discussion

Local flow dynamics in aneurysms have been studied extensively during the past few decades, and the hemodynamics in representative idealized geometries are fairly well understood. With anatomically realistic aneurysms, however, it is not necessarily straightforward to intuit the flow patterns by extrapolating from knowledge gained from idealized models alone. For example, although technically a lateral aneurysm, the present case deviated substantially from the conventional picture of flow entering the distal neck and exiting through the proximal neck, establishing a slow vortex within the aneurysm (2). Instead, the flow patterns were superficially similar to those of a large aspect ratio (ie, large depth or neck width) bifurcation aneurysm, in which high speed flow impacts the aneurysm dome obliquely, generating multiple vortices within the aneurysm (20).

The notion that aneurysm hemodynamics depend critically on geometric configuration of the aneurysm and parent vessel is, of course, not novel. The use of angiographic data as boundary conditions for CFD models of aneurysm hemodynamics has also been

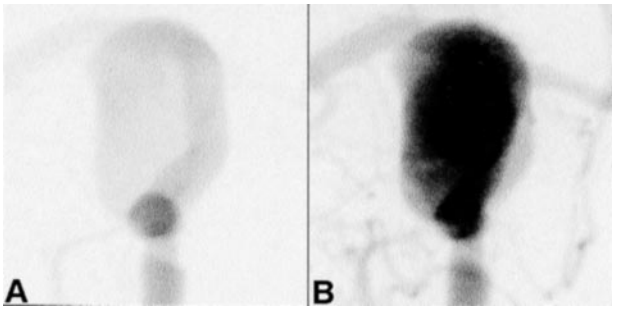

FIG 5. Two sequential frames from 2-Hz cine digital subtraction angiograms. These zoomed views correspond to the orientation and extent of the CFD model in the lower panels of Figure 2C and D.

A, Aneurysm filling dynamics, shown approximately 0.5 second after selective injection into the internal carotid artery, show good general agreement with the corresponding virtual slipstreams shown in Figure 2C.

B, One frame (ie, 0.5 second) later, the aneurysm is already largely opacified, which also is consistent with the corresponding virtual slipstreams shown in Figure 2D.

shown previously for lateral aneurysm models on the basis of single (21) or multiple (22) digital subtraction angiographic projections. The novelty of the present study is that it represents the first detailed analysis of flow dynamics in a complex human aneurysm model derived from high resolution, clinical 3D angiographic data. Such an approach now makes it possible to consider prospective studies of aneurysm hemodynamics by using what may soon be routinely available clinical imaging data. However, before such CFD analyses can be accepted at face value for use in basic or clinical studies, issues related to their validity and the underlying modeling assumptions must be considered.

Validation

Validation of image-based CFD studies of in vivo hemodynamics is a tricky proposition, because there are no "gold standard" techniques for measuring blood velocities in vivo. The ability of CFD to accurately model flow in anatomically realistic models has been shown, but only against in vitro velocity measurement in corresponding models (23–25). Although a necessary condition, this is not sufficient for showing that the computed flow patterns are representative of the in vivo hemodynamics.

To determine whether the predicted flow patterns were consistent with the in vivo hemodynamics, we exploited the inherent fluid dynamic information found in cine angiograms acquired during contrast agent injection. Specifically, comparison of the consecutive frames from cine angiography of this patient shown in Figure 5 with the corresponding times and views from Figure 2 revealed that the computed slipstream dynamics were broadly consistent with the dynamics of contrast agent filling, thus providing a qualitative but more direct validation of the computed flow dynamics. In principle, such a "reality check" could be made more quantitatively by simulating the injection of contrast agent and radiographic projection by using the CFD data and comparing the contrast agent intensity

variations extracted from clinical angiograms against those from such "virtual angiograms."

Limitations

As with any modeling study, a number of simplifying assumptions were made to render the simulation conceptually and computationally tractable. Most notable among these were the assumptions of rigid walls and Newtonian rheology, based on evidence that these are second order effects compared with the influence of geometry and flow pulsatility. In particular, numerical modeling studies conducted by Low et al (26) showed that a distensibility of 6% induced changes in secondary flow characteristics during systole in a lateral aneurysm model whereas non-Newtonian rheology was shown to have little effect on flow in a bifurcation aneurysm model (27). The broad agreement with cine angiography discussed above suggests that the modeling assumptions used in the present study provided a reasonable first order approximation to the in vivo situation. Nevertheless, higher order effects can, in principle, be included in future studies; however, some thought must be given to how patient-specific pressure waveforms, wall thickness, wall elasticity, and blood viscosity can be measured, ideally as part of a routine clinical protocol.

The important effect of flow pulsatility was captured in this study by imposing a representative periodic flow rate waveform at the model inlet. As such, the flow dynamics rendered herein represent only a "snapshot" of the hemodynamic stresses that this particular aneurysm must endure. Sustained or even transient changes in factors such as heart rate, heart rhythm, or systemic pressure would undoubtedly have some effect on the predicted flow dynamics by virtue of the changes they would induce in the inlet and outlet boundary conditions. The sensitivity of the hemodynamic environment to such changes remains incompletely understood; however, one of the chief advantages of CFD modeling is the relative ease with which boundary conditions can be altered to further study these effects.

A more practical limitation of this modeling approach pertains to the computational effort currently required for the CFD simulations. In the present case, approximately 1 week was required to run this simulation on an economic, single processor desktop workstation. Moore's eponymous law alone suggests that for the same model complexity, execution times will be down to <1 day within the next 5 years. More substantial and immediate gains can, however, be achieved by exploiting parallel processing and more intelligent "adaptive refinement" finite element meshing techniques that optimize the inherent trade-off between accuracy and speed of CFD simulations (28).

Implications for Patient Care

Clearly, exploiting improved geometric and biomechanical indices to better predict which aneurysms are at risk of rupture and to understand how and why aneurysms develop in the first place is of interest.

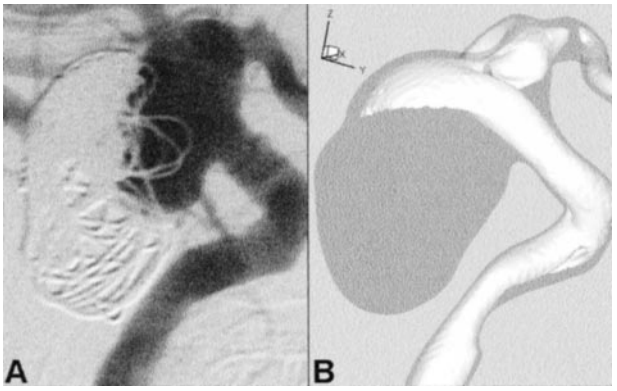

FIG 6. Illustration of a possible relationship between coil compaction and computed flow dynamics.

A, Lateral digital subtraction angiogram obtained at 6-month follow-up examination shows compaction of the coil mass away from the neck and toward the posterior wall of the aneurysm.

B, High speed flow entering the aneurysm (shown by using a 15 cm/s isovelocity surface from the cycle-averaged velocity field superimposed on a projection of the aneurysm model approximately corresponding to that in shown in *A*) is also directed toward the posterior wall of the aneurysm.

Local flow dynamics within the aneurysm lumen undoubtedly play a role in these processes but likely only as part of a complex process that includes the mechanical and biologic forces within the aneurysm wall itself. Thus, patient-specific CFD simulations alone are not likely to have an impact in these areas in the near future.

A more immediate impact on patient care is likely to be seen with the exploitation of fluid dynamic information in the area of endovascular aneurysm therapy. As noted in the Introduction, the success of techniques such as coiling and stent placement depends critically on the ability to control the local fluid dynamic environment. A general understanding of how such devices alter flow patterns has been gained mainly through experimental studies (2, 3, 6, 29, 30); however, CFD studies have recently been attempted (31, 32). The latter study of a coiled basilar tip aneurysm is of particular interest for its attempt to incorporate patient-specific geometry and flow data. Unlike the present study, however, no attempt was made to construct a detailed anatomic representation of the aneurysm and parent vessel geometry. Instead, an *approximate* model was constructed from geometric primitives (ie, a sphere and cylinders) the dimensions and orientations of which were derived from a patient's CT angiogram.

The ability to predict the fluid dynamic forces associated with a *particular* intervention could assist clinical decision making regarding the selection of the most appropriate treatment strategy and the design and early testing of novel endovascular devices. To illustrate this in the context of the present study, we note that coil compaction was observed for this patient at a routine 6-month follow-up examination. As shown in Figure 6, the configuration of the compacted coils was consistent with the predicted trajectory of high speed flow entering the aneurysm and impacting the coil mass. Although admittedly post

hoc speculation, this nevertheless evokes the type of prospective, patient-specific analysis that could be validated against clinical outcome and ultimately used in a predictive manner to improve the outcome of aneurysm therapies.

Future Directions

Having shown that patient-specific CFD analyses are *possible*, the onus is now on researchers to bring these technologies into a clinical setting. In addition to the obvious technologic need—namely, more powerful computing—this will require more sophisticated and automated techniques for converting the image information into a CFD model and more effective ways of communicating the complex flow dynamics to clinicians (33). Minor extensions to routine radiologic protocols for patients with aneurysms will also be needed to acquire the patient-specific flow rate information (eg, by using MR imaging or Doppler sonography) and the higher frame rate cine angiograms needed to validate the CFD models before their use in a predictive capacity. Finally, novel CFD modeling strategies will be required to automatically and efficiently resolve the details of flow around fine devices such as stents and coils realistically embedded into patient-specific CFD models of cerebral aneurysms.

Conclusion

This study has presented the first prospective analysis of patient-specific aneurysm hemodynamics derived from high resolution, in vivo 3D angiography and CFD. Predicted flow patterns within the aneurysm were highly complex but were consistent with cine angiography and also with the subsequent compaction of coils. Our results illustrate the importance of anatomic realism in determining the resulting flow dynamics, and our techniques serve as the first key step toward incorporating patient-specific fluid dynamic information into a clinical setting.

As 3D angiographic techniques become more commonly used in the clinic, we can envision the routine acquisition of sufficiently high resolution angiographic datasets for large scale prospective or even retrospective studies of aneurysm hemodynamics and subsequent clinical outcomes. The ability to acquire high frame rate angiograms during the same clinical examination provides a unique opportunity to validate the predictive capabilities of these models. With continuing improvements in automated image analysis tools and computational performance, it will eventually be possible to perform these simulations in time frames suitable for clinical decision making.

References

1. Burleson AC, Turitto VT. **Identification of quantifiable hemodynamic factors in the assessment of cerebral aneurysm behavior: on behalf of the Subcommittee on Biorheology of the Scientific and Standardization Committee of the ISTH.** *Thromb Haemost* 1996; 76:118–123
2. Graves VB, Strother CM, Partington CR, Rappe A. **Flow dynamics of lateral carotid artery aneurysms and their effects on coils and balloons: an experimental study in dogs.** *AJNR Am J Neuroradiol* 1992;13:189–196
3. Gobin YP, Counord JL, Flaud P, Duffaux J. **In vitro study of haemodynamics in a giant saccular aneurysm model: influence of flow dynamics in the parent vessel and effects of coil embolisation.** *Neuroradiology* 1994;36:530–536
4. Lieber BB, Gounis MJ. **The physics of endoluminal stenting in the treatment of cerebrovascular aneurysms.** *Neurol Res* 2002;24[suppl 1]:S33–S42
5. Liou TM, Liou SN. **A review on in vitro studies of hemodynamic characteristics in terminal and lateral aneurysm models.** *Proc Natl Sci Counc Repub China B* 1999;23:133–148
6. Imbesi SG, Kerber CW. **Analysis of slipstream flow in a wide-necked basilar artery aneurysm: evaluation of potential treatment regimens.** *AJNR Am J Neuroradiol* 2001;22:721–724
7. Steinman DA. **Image-based computational fluid dynamics modeling in realistic arterial geometries.** *Ann Biomed Eng* 2002;30:483–497
8. Fahrig R, Fox AJ, Lownie S, Holdsworth DW. **Use of a C-arm system to generate true three-dimensional computed rotational angiograms: preliminary in vitro and in vivo results.** *AJNR Am J Neuroradiol* 1997;18:1507–1514
9. Ladak HM, Milner JS, Steinman DA. **Rapid three-dimensional segmentation of the carotid bifurcation from serial MR images.** *J Biomech Eng* 2000;122:96–99
10. Milner JS, Moore JA, Rutt BK, Steinman DA. **Hemodynamics of human carotid artery bifurcations: computational studies with models reconstructed from magnetic resonance imaging of normal subjects.** *J Vasc Surg* 1998;28:143–156
11. Minev PD, Ethier CR. **A characteristic/finite element algorithm for the 3-D Navier-Stokes equations using unstructured grids.** *Comput Methods Appl Mech Eng* 1999;178:39–50
12. Ethier CR, Steinman DA, Ojha M. **Comparisons between computational hemodynamics, photochromic dye flow visualization and magnetic resonance velocimetry.** In: Xu XY, Collins MW, eds. *The Haemodynamics of Arterial Organs: Comparison of Computational Predictions with in Vivo and in Vitro Data.* Southampton: WIT Press; 1999:131–183
13. Ethier CR, Prakash S, Steinman DA, Leask RL, Couch GG, Ojha M. **Steady flow separation patterns in a 45 degree junction.** *J Fluid Mech* 2000;411:1–38
14. Frayne R, Steinman DA, Ethier CR, Rutt BK. **Accuracy of MR phase contrast velocity measurements for unsteady flow.** *J Magn Reson Imaging* 1995;5:428–431
15. Imbesi SG, Kerber CW. **Analysis of slipstream flow in two ruptured intracranial cerebral aneurysms.** *AJNR Am J Neuroradiol* 1999;20: 1703–1705
16. Kerber CW, Heilman CB. **Flow in experimental berry aneurysms: method and model.** *AJNR Am J Neuroradiol* 1983;4:374–377
17. Kerber CW, Hecht ST, Knox K, Buxton RB, Meltzer HS. **Flow dynamics in a fatal aneurysm of the basilar artery.** *AJNR Am J Neuroradiol* 1996;17:1417–1421
18. Kerber CW, Imbesi SG, Knox K. **Flow dynamics in a lethal anterior communicating artery aneurysm.** *AJNR Am J Neuroradiol* 1999;20: 2000–2003
19. Tambasco M, Steinman DA. **On assessing the quality of particle tracking through computational fluid dynamic models.** *J Biomech Eng* 2002;124:166–175
20. Ujiie H, Tachibana H, Hiramatsu O, et al. **Effects of size and shape (aspect ratio) on the hemodynamics of saccular aneurysms: a possible index for surgical treatment of intracranial aneurysms.** *Neurosurgery* 1999;45:119–130
21. Gonzalez CF, Cho YI, Ortega HV, Moret J. **Intracranial aneurysms: flow analysis of their origin and progression**. *AJNR Am J Neuroradiol* 1992;13:181–188
22. Harreld MR, Valentino DJ, Karplus WJ. **The virtual aneurysm: virtual reality in endovascular therapy.** *Stud Health Technol Inform* 1996;29:12–20
23. Perktold K, Hofer M, Rappitsch G, Loew M, Kuban BD, Friedman MH. **Validated computation of physiologic flow in a realistic coronary artery branch.** *J Biomech* 1998;31:217–228
24. Botnar R, Rappitsch G, Scheidegger MB, Liepsch D, Perktold K, Boesiger P. **Hemodynamics in the carotid artery bifurcation: a comparison between numerical simulations and in vitro MRI measurements.** *J Biomech* 2000;33:137–144
25. Myers JG, Moore JA, Ojha M, Johnston KW, Ethier CR. **Factors influencing blood flow patterns in the human right coronary artery.** *Ann Biomed Eng* 2001;29:109–120

26. Low M, Perktold K, Raunig R. **Hemodynamics in rigid and distensible saccular aneurysms: a numerical study of pulsatile flow characteristics.** *Biorheology* 1993;30:287–298
27. Perktold K, Peter R, Resch M. **Pulsatile non-Newtonian blood flow simulation through a bifurcation with an aneurysm.** *Biorheology* 1989;26:1011–1030
28. Prakash S, Ethier CR. **Requirements for mesh resolution in 3D computational hemodynamics.** *J Biomech Eng* 2001;123:134–144
29. Lieber BB, Stancampiano AP, Wakhloo AK. **Alteration of hemodynamics in aneurysm models by stenting: influence of stent porosity.** *Ann Biomed Eng* 1997;25:460–469
30. Boecher-Schwarz HG, Ringel K, Kopacz L, Heimann A, Kempski O. **Ex vivo study of the physical effect of coils on pressure and flow dynamics in experimental aneurysms.** *AJNR Am J Neuroradiol* 2000;21:1532–1536
31. Aenis M, Stancampiano AP, Wakhloo AK, Lieber BB. **Modeling of flow in a straight stented and nonstented side wall aneurysm model.** *J Biomech Eng* 1997;119:206–212
32. Groden C, Laudan J, Gatchell S, Zeumer H. **Three-dimensional pulsatile flow simulation before and after endovascular coil embolization of a terminal cerebral aneurysm.** *J Cereb Blood Flow Metab* 2001;21:1464–1471
33. Lee D, Valentino DJ, Duckwiler GR, Karplus WJ. **Automatic skeleton generation for visualizing 3D, time-dependent fluid flows: application to the virtual aneurysm.** *Stud Health Technol Inform* 2001;81:272–278